The Effects of Different Drivers on the Induced Martian Magnetosphere Boundary: A Case Study of September 2017

C. L. Lentz[1], D. N. Baker[1], L. Andersson[1], S. Thaller[1], C. Fowler[2], T. W. Leonard[1]

[1]Laboratory for Atmospheric and Space Physics, University of Colorado, Boulder, CO, USA.
[2]Space Sciences Laboratory, University of California, Berkeley, CA, USA.

Key Points:

- The ICME during September 2017 had no statistically significant impact on the IMB standoff location.
- The magnetic pressure of the Magnetic Pileup Region (MPR) and the thermal pressure in the ionosphere had the greatest influence on the IMB standoff distance.

Corresponding author: Christy Lentz , christy.lentz@lasp.colorado.edu

Abstract

The Magnetic Pileup Boundary or Induced Magnetosphere Boundary (IMB) has been an enigma in Mars aeronomy. Previously dubbed the planetopause, magnetopause, ion-composition boundary, and protonopause, identification of this unique plasma region has been marked by difficulty. In this case study, we used data from the Mars Atmosphere and Volatile EvolutioN (MAVEN) mission to identify IMB crossings and configurations during the month of September 2017 with a particular focus on the 10 September 2017 solar events. It was concluded that the ICME had no statistically significant impact on the IMB standoff locations. This study also investigated the effects of upstream dynamic pressure, thermal pressure from the magnetosheath, magnetic pressure from the Magnetic Pileup Region (MPR), thermal pressure associated with the ionosphere, and Extreme Ultraviolet (EUV) irradiance on the IMB during September 2017. We have found that during the 163 IMB crossings, magnetic pressure in the MPR and thermal pressure in the ionosphere had the largest influence on the IMB standoff distance.

Plain Language Summary

The plasma environment of Mars is a dynamic and complex place. There are multiple layers and confines of plasma formed from the interaction of plasma from planetary origin and the plasma of the solar wind. One such complicated plasma boundary is the Induced Magnetosphere Boundary (IMB) which is one of many located in the solar wind/ionosphere interface region. The IMB is widely known to be affected by solar wind dynamic pressure and solar irradiance flux. However, there are other pressures that sway the position and shape of the IMB as well. September 2017 brought about an intense pressure event due to the solar eruptive activity. All aspects of the Martian plasma environment were affected. We therefore took this opportunity to examine how the IMB reacted to different plasma pressures brought about by the solar events. We also tried to determine which pressure(s) were the most influential in determining the IMBs standoff distance.

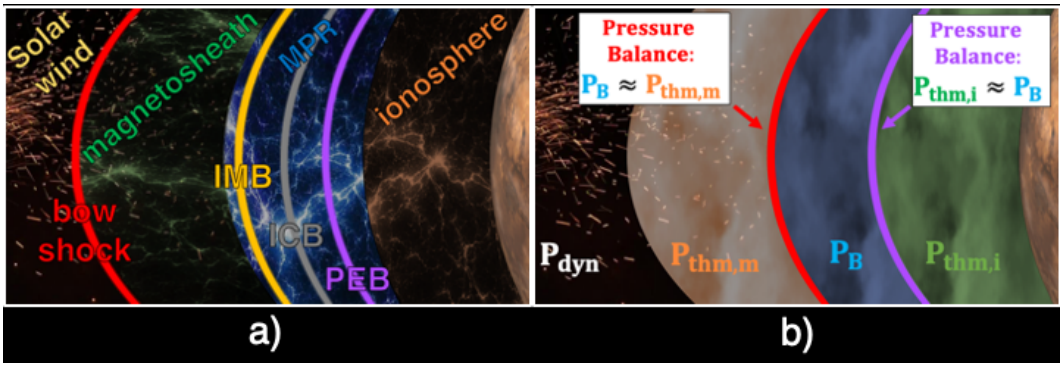

Figure 1. Diagrams of the dayside induced Martian magnetosphere (i.e., from the ionosphere to the foreshock). **a)** The distinct plasma regions (rotated text) and plasma boundaries (horizontal text). **b)** The induced Martian magnetosphere split up by predominant pressure terms.

1 Introduction

1.1 Mars Aeronomy

The Mars plasma environment is in a constant state of fluctuation. As solar wind bombards the planet, and interacts directly with the upper atmosphere, an assortment of plasma zones form as a result. The various plasma regions and boundaries are represented in Figure 1a) for the dayside induced Martian magnetosphere. In this general scenario, the Martian plasma environment is experiencing no high dynamic pressure event, nor is anything being perturbed by underlying crustal magnetic. One way to define general regions of the induced Martian magnetosphere is by location of dominant pressure terms, as symbolized in Figure 1b). Going radially inward into the induced magnetosphere, just before entering, there is an upstream region where solar wind dynamic pressure dominates (P_{dyn} in Figure 1b). Thereafter is the bow shock. This shock wave slows down the solar wind from supersonic to subsonic speeds (Mazelle et al., 2004). Following is the magnetosheath which is characterized by shocked solar wind particles, and thermal pressure ($P_{thm,m}$) dominating both magnetic (P_B) and dynamic pressures. In the magnetosheath, one can also see low amplitude magnetic fields with high wave activity. From the start of the magnetosheath to the start of the ionosphere, the overall composition of the plasma goes from being composed of primarily light solar wind ions, to being composed of heavy planetary ions (Halekas et al., 2018).

The average altitude where the thermal pressure of the magnetosheath balances the magnetic pressure of the magnetic pileup region (MPR) is one of the pressure balance boundaries ($P_B \approx P_{thm,m}$). The MPR exhibits strong magnetic fields caused by the draping of the interplanetary magnetic field about the ionosphere (Ma et al., 2008). Going further in, the fluctuating magnetic field then begins to transition to a more draped magnetic field configuration, and the Magnetic Pileup Boundary (MPB), also known as the Induced Magnetosphere Boundary (IMB) is then reached (Vignes et al., 2000). Also around this area, magnetic field fluctuations and energetic electrons reduce in magnitude (Acuña et al., 1998; Bertucci et al., 2003, 2005). Continuing on, the Ion Composition Boundary (ICB; Sauer et al., 1994, 1995) is then encountered. Here a sharp drop in solar wind proton fluxes over a relatively small distance occurs, and an increase in planetary heavy ions, mainly O^+ and O^{+2}, appears (Breus et al., 1991). Next is the Photoelectron boundary (PEB; Mitchell et al., 2000, 2001) at the external limit of the ionosphere, where CO_2 20-30 eV photoelectrons disappear from the electron spectra (Garnier et al., 2017). Further in emerges another pressure balance boundary ($P_{thm,i} \approx P_B$) where the thermal pressure corresponding to the ionosphere balances the magnetic pressure in the MPR (Xu et al., 2016). Below this is the ionosphere where thermal pressure is the leading pressure term (Holmberg et al., 2019).

Of these several plasma boundaries, we chose to investigate the inner workings of the Induced Magnetosphere Boundary, also called the Magnetic Pileup Boundary (MPB; Nagy et al., 2004; Crider et al., 2000), the "boundary layer" (Dubinin et al., 1996), and many more as described in Espley (2018). This study will use the term Induced Magnetosphere Boundary (IMB) as depicted in gold in Figure 1a). The IMB is defined simply as the region where magnetic field fluctuations are reduced, and there is an attenuation in electron flux around the 20-90 eV energy range.

The purpose of this study was to examine the IMB response to the ICME, increased plasma pressures, and solar EUV flux during September 2017. For 163 orbits, we identified a mixture of dayside and nightside IMB crossings by using the root mean square (RMS) of the magnetic field amplitude and electron energy flux signatures. We calculated correlations and performed simple and multiple regression analyses between the IMB standoff distances and estimated upstream dynamic pressure, the solar irradiance, the thermal pressure in the magnetosphere and ionosphere, and the magnetic pressure in the MPR.

1.2 Mars during September 2017

Mars saw elevated space weather activity during September 2017. On 9 September 2017, two slow Coronal Mass Ejections (CMEs) erupted at the Sun and merged while in transit. On 2017-09-10/15:54:34 UTC a third faster CME erupted at the Sun. It coalesced with the other CMEs to form a triple-merged Interplanetary Coronal Mass Ejection (ICME). The ensuing events were cause for excitement as examining the Martian plasma environment during this period provided valuable insight as to what extent solar wind forcing affects the properties of various plasma regions.

The a detailed account of the September 2017 events can be found in Lee et al. (2018). The events that had the greatest influence on the IMB included a fast-solar wind stream and its corresponding Stream Interaction Region collision with Mars at 2017-09-10/23:30:00 UT. Subsequently, IMF draping down to 300 km was seen at 2017-09-11/02:34. At $\sim$ 2017-09-13/02:52 UT the ICME collided with Mars. The deepest draped field penetration was seen after the ICME shock arrival at 2017-09-13/02:52:13 UT. With the enhanced dynamic pressure from the ICME encounter, the draped IMF penetrated down to 200 km into the Martian atmosphere over the northern hemisphere. Harada et al. (2018) deduced from MAG data that during the ICME encounter, the magnitude of the magnetic field showed a significant enhancement over a wide range of Solar Zenith Angles.

2 IMB Crossing Identifications

We now define some terminology used in this Study. One orbit during September 2017 consisted of MAVEN passing through the inbound IMB, reaching periapsis, beginning its outbound orbit, and finally passing through the outbound IMB. The majority of the outbound IMB crossings were located on the nightside, while the majority of the inbound IMB crossings took place on the dayside. Sample sizes of the inbound dayside IMB and outbound nightside IMB were largest, and therefore were used for the rest of the study. A distinction is made between dayside and nightside crossings as nightside IMB crossings are found to be more variable than dayside crossings (Nagy et al., 2004).

An example of the IMB location identifications for one orbit is displayed in Figure 2. Electron fluxes were measured by MAVEN's Solar Wind Electron Analyzer (SWEA; Mitchell et al., 2016). SWEA's electron fluxes for the 27.5- to 78.4-eV energy ranges demonstrated the most dramatic attenuation as contrasted with other energy ranges and were

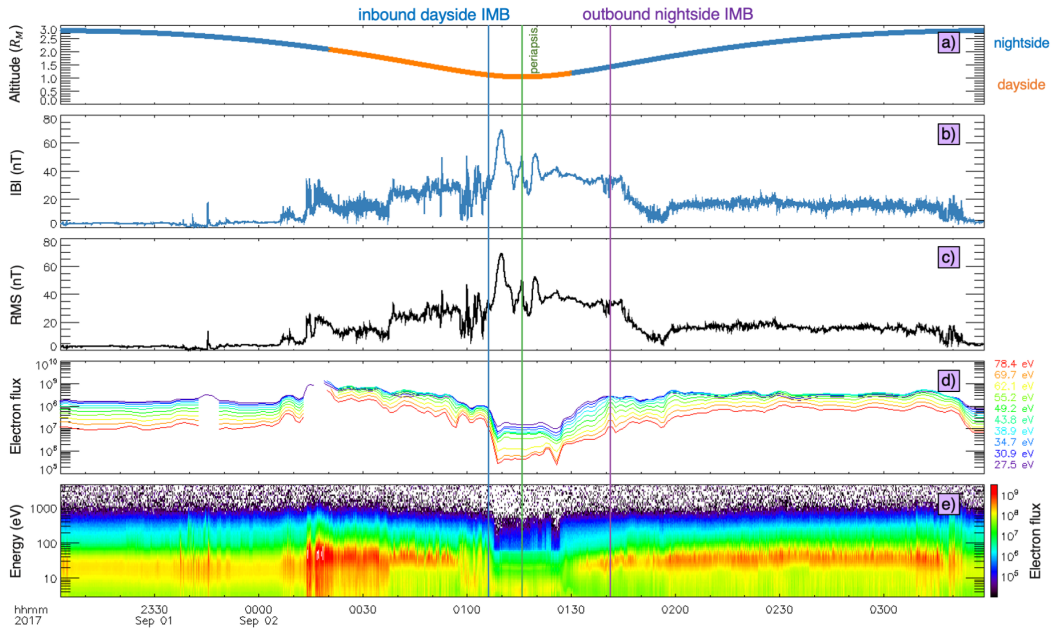

Figure 2. Example IMB identifications. Panel a) MAVEN's position in MSO coordinates determined from LPW. Panel b) Magnitude of the magnetic field (nT). Panel c) RMS of the magnitude of the magnetic field (nT). Panel d) electron energy fluxes ($cm^{-2}s^{-1}sr^{-1}$) for the specified energy ranges. Panel e) electron energy flux of all energy ranges. Blue and purple vertical lines represent IMB crossings.

therefore used as a basis for identification (Figure 2d). We also used 1s averaged magnetic field vector data from MAVEN's magnetometer (MAG; Connerney et al., 2015) (Figure 2b). The IMB was located in the data sets as the boundary where fluctuations of the magnetic field and the electron energy fluxes decreased from values common in the magnetosheath, to values inherent to the induced magnetosphere. Magnetic field fluctuations were characterized using the root-mean-square (RMS) value of the magnitude of the magnetic field every 8 seconds (Acuña et al., 1998). The identification processes for the inbound and outbound IMB are listed as follows.

To identify the inbound IMB each orbit, the electron flux and RMS of the magnetic field magnitude from apoapsis to periapsis were used. There were two criteria that had to be met simultaneously to be considered an inbound IMB crossing. Firstly, the average flux attenuation in each energy range had to be at least a factor of 1.8 over a 200 km altitude drop. Secondly, the RMS of the magnetic field magnitude had to decrease by a factor greater than 1.1 over a 200 km altitude drop or more. The altitudes of the inbound IMB locations were extrapolated from the MSO coordinates calculated by the Langmuir Probe and Waves (LPW; Andersson et al., 2015). A minimum 200 km altitude change was imposed to ensure there was no double boundary crossings. In total, there were 141 inbound crossings that took place on the dayside (in front of the terminator), and 22 that took place on the nightside.

The outbound IMB was identified using the electron flux and RMS of the magnetic field magnitude time series data from periapsis to apoapsis. Again, two simultaneous criteria had to be met. Firstly, each energy range had to show a rapid flux enhancement of a factor of 1.8 or more and maintain this enhancement for at least a 200 km altitude increase. Secondly, The RMS of the magnetic field magnitude had to increase by a factor greater than 1.1 over a minimum 200 km altitude increase. The outbound IMB was the average time when each of the energy ranges and RMS began to show rapid enhancements. There were 35 dayside outbound IMB crossings, and 128 nightside crossings.

3 Data Analysis

3.1 Upstream Dynamic, Thermal, and Magnetic Pressure, and Solar Irradiance Effects on the IMB

We next investigated the main drivers that could affect the IMB. The dayside inbound IMB and nightside outbound IMB were chosen as our primary data sets. Further discussion of dayside IMB refers to the dayside inbound IMB, and nightside IMB refers to the nightside outbound IMB data set. Edberg et al. (2008) showed that crustal remnant magnetic fields can perturb the IMB $\sim 0.10\ R_M$ father out in the Southern Hemisphere. Yet, MAVEN's orbit during September 2017 was such that crustal fields were passed over during times of apoapsis. We therefore considered these effects on the standoff distance to be negligible.

Previous studies (e.g., Brain et al., 2010; Crider et al., 2000; Dubinin et al., 2008; Matsunaga et al., 2017) showed that factors such as the magnetic pressure, dynamic pressure, and thermal pressure all contribute to the pressure balance in the plasma environment around Mars. Similarly, solar EUV flux was also found to cause Martian plasma boundary locations extend or contract (Edberg et al., 2009). To compare the IMB altitudes during September 2017, the thermal pressure in the magnetosphere ($P_{thm,m}$), the magnetic pressure associated with the MPR (P_B), and the thermal pressure of the ionosphere ($P_{thm,i}$) were calculated.

The total magnetic pressure was defined as:

$$P_B = \frac{|B|^2}{2\mu_0}$$

Where $|B|$ is the magnitude of the magnetic field vector, and μ_0 is the permeability of free space constant. The thermal pressure of the magnetosheath is then:

$$P_{thm,m} = n_i k_B T_i$$

where n_i is the density of ions, k_B is the Boltzmann constant, and T_i is the temperature of ions as measured by MAVEN's Solar Wind Ion Analyzer (SWIA; Halekas et al., 2015). The thermal pressure prevalent in the ionosphere is:

$$P_{thm,i} = 2n_e k_B T_e$$

where n_e is the electron density, and T_e is the temperature of the electrons as measured by LPW.

Table 1. Correlation statistics and simple regression analysis for the IMB and P_{dyn}, $P_{thm,m}$, P_B, $P_{thm,i}$, and 65.5 nm EUV flux.

		CC	P-value	Equation	SSE	Adj. R^2	RMSE
Function of P_{dyn}	dayside IMB	0.13	0.39	$-0.06x^7 + 0.50x^6 - 1.36x^5 + 0.93x^4 + 1.06x^3 - 1.13x^2 - 0.15x + 0.64$	2.46	0.14	0.24
	nightside IMB	-0.35	0.03	$0.08x^3 - 0.31x^2 - 0.06x + 0.89$	6.47	0.12	0.43
Function of $P_{thm,m}$	dayside IMB	0.13	0.12	$-0.01x^6 + 0.08x^5 - 0.38x^4 + 0.48x^3 + 0.18x^2 - 0.35x + 0.55$	403	0.14	1.73
	nightside IMB	0.01	0.87	$5.24\text{e-}05x^{-2.16} + 0.96$	1099	0.14	2.97
Function of P_B	dayside IMB	-0.53	0.00	$-0.01x^5 + 0.13x^4 - 0.45x^3 + 0.54x^2 - 0.18x + 0.21$	3.06e03	0.50	4.76
	nightside IMB	-0.25	0.00	$0.23x^{-0.32} - 0.04$	5.24e03	0.61	6.48
Function of $P_{thm,i}$	dayside IMB	-0.55	0.00	$-0.85x^{0.15} + 0.66$	195.33	0.71	1.19
	nightside IMB	-0.41	0.00	$-1.30x^{0.13} + 1.06$	545.97	0.56	2.09
Function of 65.5 nm EUV flux	dayside IMB	0.54	0.00	$-0.01x^5 + 0.09x^4 - 0.07x^3 - 0.24x^2 + 0.30x + 0.51$	63.54	0.41	0.69
	nightside IMB	0.42	0.00	$-0.04x^3 + 0.05x^2 + 0.28x + 0.79$	188.08	0.21	1.23

The dynamic pressure of the solar wind can be easily calculated from SWIA, but for September 2017, only sparse solar wind coverage was attained. MAVEN's orbital orientation resulted in its apoapsis location never extending beyond the nominal bow shock. To achieve a more complete data set, we averaged SWIA's proxy and actual measurements, MEX/ASPERA-3 Ion Mass Analyzer (IMA; Barabash et al., 2006) measurements, and the Wang-Sheeley-Arge (WSA)-Enlil model (hereafter, WSA-Enlil; Arge et al., 2004; Odstrcil, 2003). This produced a dynamic pressure data set from 8 September 2017 to 18 September 2017 with an hourly cadence.

MAVEN's Extreme Ultraviolet Monitor (EUVM; Eparvier et al., 2015) instrument provided the solar irradiance measurements. The modeled full spectral irradiance in 1-nm bins from 0-190 nm were all compared to the IMB locations. The 65.5 nm wavelength showed the most cause-and-effect relationship, and therefore was included as a factor in determining what affected each boundary's position.

After obtaining comparable data sets, we wanted to understand if each plasma pressure and solar EUV flux term (driving factors) directly affected the dayside and nightside IMB (response variables). If there was a clear effect, then we wanted to be able to quantify it. To do this, we calculated correlation coefficients between each driving factor and IMB location to establish any linear correlation between the variable pairs. Simple regression analysis was employed to model any casual effects of each driving factor on the IMB altitudes. Model fit statistics are listed in Table 1.

To investigate the interrelation between the predictor variables and the IMB locations, the Pearson correlation coefficient (CC) and its P-value were. A CC of -1.0 shows a perfect negative correlation, a CC of 1.0 shows a perfect positive correlation, and a CC

of 0.0 shows no association. P-values were used to test the hypothesis that there was no relationship between the observed phenomena and the predictor variables (null hypothesis). P-values range from 0 to 1, where values lower than the 0.05 standard significance level have a low probability of observing the null hypothesis. The dayside IMB had no linear association with P_{dyn} nor $P_{thm,m}$. The nightside IMB showed no linear association with $P_{thm,m}$.

Models for each driving factor and IMB location were fit by using simple regression analysis, i.e., regression analysis involving only two variables. The dependent (response) variables were the dayside and nightside IMB. The independent (predictor) variables were P_{dyn}, $P_{thm,m}$, P_B, $P_{thm,i}$, and 65.5 nm EUV flux. Power, rational, polynomial, and exponential functions were all tried as potential relational equations. The goodness of fit for each model was assessed by three main components. The first being the sum of squares due to error (SSE) that measures the total deviation of the modeled response values to the actual IMB values. Values closer to 0 indicate a smaller random error component in the model, and that the fit will be more useful for prediction. The second is the adjusted R^2. It uses the R^2 value and adjusts it based on the residual degrees of freedom for each case. Values range from 0 to 1, where 1 demonstrates that a greater proportion of variance is accounted for by the model. The final statistic is the Root Mean Squared Error (RMSE) which supplies insight into how close the observed data points are to the model's predicted values. Values closer to 0 show better fits. (Kutner et al., 2005). The dayside IMB as a function of $P_{thm,i}$ resulted in the best fit out of all the variable pairs. The correlation coefficient also implied that the dayside IMB generally shrunk as $P_{thm,i}$ increased.

3.2 Multiple Regression Analysis of P_B, $P_{thm,i}$, and 65.5 nm EUV flux on IMB Locations

The IMB configuration is a result of multiple forcing factors. By resolving which individual variables had the most control over the IMB, a better model could be built using only the most influential variables. Multiple nonlinear regression models (MNRM) were used to evaluate how P_B, $P_{thm,i}$, and 65.5 nm EUV FISM jointly influence each IMB standoff distance. Driving factors that produced an adjusted R^2 value below 0.20 during the simple regression analyses (Table 1) were excluded from the MNRM. This included $P_{thm,m}$ and P_{dyn}.

Models that produced the best fits from the simple regression analysis were pieced together to form each MNRM. Again, RMSE and adjusted R^2 values were used as fit statistics. The F-statistic vs. a constant model and its associated P-value were also used to evaluate each fit. The F-statistic vs. a constant model produces a value ranging from 0 to an arbitrary number that tells you whether the supplied model fits the data better than a constant model, i.e., a model with no independent variables. Larger values represent greater dispersion in the IMB altitudes. The P-value also must be considered, as the P-value is the probability that the F-statistic could have been produced by chance. An adequate fit of the dayside and nightside IMB would produce a P-value that is lower than the 0.05 significance level, and an F-statistic greater than 0. For a detailed explanation on using regression analysis in planetary data, see Chattopadhyay and Chattopadhyay (2014).

The equation of best fit for the dayside IMB was $-25.53(P_B)^5+73.50(P_B)^4-74.05(P_B)^3+31.22(P_B)^2-5.22(P_B)-0.53(P_{thm,i})^{0.16}-0.01(EUV)^5+0.09(EUV)^4-0.07(EUV)^3-1.28e09(EUV)^2+1.28e06(EUV)$, with a RMSE of 4.04, an adjusted R^2 of 0.69, a F-stat vs. constant model value of 44.7, and a corresponding P-value of 5.74e-32. The nightside IMB was approximated by $0.05(P_B)^{-0.52}-0.63(P_{thm,i})^{0.16}-0.01(EUV)^2+2.41e06(EUV)-0.87$. The associated RMSE was 5.94, adjusted R^2 value was 0.71, F-stat vs. constant model value was 79.1 with a P-value of 4.39e-33.

The limited observations of the dayside and nightside IMB made it difficult to examine its response to each event of interest. The MNRM made it possible to predict the IMB altitude at the exact time when $P_{thm,i}$, P_B, and the 65.5 nm wavelength EUV FISM reached their maximum values. The predicted IMB altitudes are plotted in Figure 3. Negative prediction values were excluded from the plots. Times when plasma pressures and EUV flux reached their maximums are plotted as vertical lines. The red line at 2017-09-09/10:35:12 represents $P_{thm,i}$ reaching its maximum value of 2.07 nPa. The orange line at 2017-09-10/16:11:30 is when the solar EUV irradiance peaked. The green line at 2017-09-13/06:00:00 is the estimated time when P_{dyn} reached a maximum 4.45 nPa. The cyan line at 2017-09-13/07:12:07 signifies $P_{thm,m}$ peaking at 6.31 nPa. The black vertical line at 2017-09-13/07:55:51 marks the P_B maximum value of 16.75 nPa. The tan shaded region represents the disturbed magnetosphere conditions that spanned from the arrival of the ICME on 2017-09-13, to when conditions returned to normal around 2017-09-15.

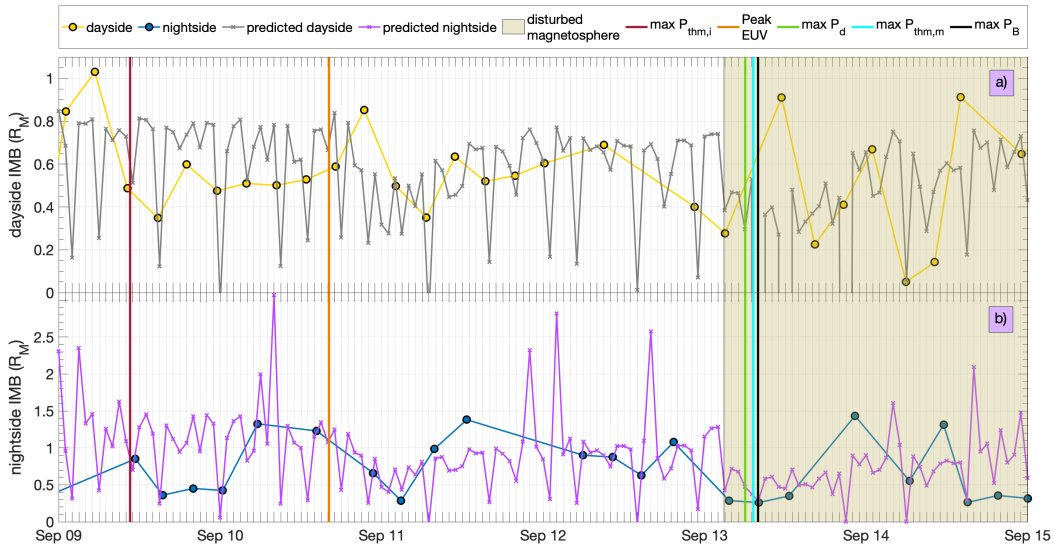

Figure 3. Dayside and nightside IMB altitudes from 2017-09-09 to 2017-09-15. Included are the events of interest indicated by vertical lines, and the MNRM predicted IMB values.

4 Discussion and Conclusions

The purpose of this study was to understand how the IMB changed in response to the heightened solar activity in September 2017. The solar flare lead to enhanced solar EUV flux, and the merged ICME brought about intense dynamic and magnetic pressure which, as an input into the Martian plasma environment, all affected the IMB. A cursory examination of the distribution of standoff distances before, during, and after the disturbed magnetosphere conditions showed that the ICME had no considerable influence on the dayside and nightside IMB location. The dayside and nightside IMB decreased in altitude immediately after the onset of the merged ICME. However, the IMB was witnessed reaching lower altitudes both before and after the disturbed magnetosphere period. This led to the question that if the merged ICME did not have an instant effect on the IMB, what driving factor did? The individual relationships between plasma pressures and solar irradiance and the IMB were probed to ascertain which factor had the greatest influence on the IMB (Table 1). Using simple regression analysis, we found that $P_{thm,i}$ and P_B had the most statistically significant relationship with the dayside and nightside IMB. P_{dyn} and $P_{thm,m}$ showed relatively weak influences on the standoff distances. The brief time period that data was available for P_{dyn} can be a contributing factor to the inability to detect more of a trend between P_{dyn} and the IMB locations. Also,

it is possible that the WSA-ENLIL cone model did not delineate the true upstream dynamic pressure values.

Building on simple regression models, we used MNRMs to characterize the complex nature of the IMB as functions of the most influential driving factors (Figure 3). This resulted in fits for the IMB that incorporated P_B, $P_{thm,i}$ and the 65.5 nm wavelength solar irradiance. We calculated that the dayside IMB MNRM predicted the correct IMB altitude within a 95% confidence interval 62% of the time. The nightside IMB MNRM predicted the correct IMB altitude within a 95% confidence interval 55% of the time. The nightside IMB was described by a more simplistic MNRM that included fewer terms in the equation, and a higher adjusted R^2 value. Examining Figure 3, dayside and nightside IMB values were known within a one hour window of each event of interest, however we did not have exact IMB altitudes at the times of high pressure and peak EUV events. We therefore used MNRM to produce IMB approximations with a 1 minute cadence. Both models captured the general trend of the IMB being negatively correlated to $P_{thm,i}$, and P_B, while being positively correlated with EUV flux for the maximum pressure and EUV flux events. The adjusted R^2 values of the dayside and nightside MNRM proved that the models explain 69%, and 71% of the variability in the IMB altitudes, respectively.

One interesting point is the estimated dayside IMB altitude at the maximum P_B. The model approximated a negative altitude of -5.24e+05 R_M, which obviously is impossible. Yet this decrease in altitude is reminiscent of a well-known phenomenon. The compression of the dayside IMB is expected as dynamic pressure is known to be a main driver of boundary. As the dynamic pressure pushes the IMB downward to Mars, the magnetic flux piled up in front of the planet must be stored in a smaller volume, thus causing the magnetic pressure to reach such high values(Edberg et al., 2008). Since the magnetic pressure has a noteworthy impact on the IMB, it would cause a large compression. The only two IMB data points around this time are at 2017-09-13/03:02:20 (0.28 R_M) and at 2017-09-13/11:26:16 (0.91 R_M). The model properly suggests that there is a decrease directly following the high dynamic and magnetic pressure events, but it does not estimate the proper value. After an expected compression, the dayside IMB then jumps in altitude as the plasma pressures return to equilibrium. This is where the model does not capture this increase. This is due to the absence of dynamic pressure as a predictor variable for the dayside IMB. It is accepted that the Martian ionosphere is magne-

tized during times of high solar wind pressure. The magnetic pressure associated with the resulting ionospheric field can supplement the ionospheric thermal pressure and push upward on the overlying MPR magnetic pressure (Nagy et al., 2004). This phenomenon explains why the dayside IMB expanded after the plasma environment experienced a high dynamic pressure input, and why the model failed to capture it.

September 2017 marked an exciting period for all spacecraft in operation around Mars to receive valuable observations of how the plasma regions respond to such input. Future research will be aimed at better understanding the intricate relationship between the IMB, PEB, ICB, and the pressure balance boundaries for extended time periods. This includes examining seasonal trends and relationships. The IMBs dependence on geographical configurations such as the input from strong crustal magnetic fields will also be another line of inquiry. As the upstream interplanetary plasma and its embedded field can now be monitored by multiple spacecraft; it is only a matter of time until the full nature of the IMB and other Martian plasma regions can be deduced.

Acknowledgments

The MAVEN mission has been made possible through NASA sponsorship and the dedicated efforts of NASA Goddard Space Flight Center, LASP, Lockheed Martin, and the MAVEN Technical and Science Teams. The MAVEN data shown are publicly available at the NASA Planetary Data System website (http://ppi.pds.nasa.gov). The WSA-Enlil simulation results (run name "Leila_Mays_120817_SH_9") were provided by the NASA/GSFC Community Coordinated Modeling Center through their public Runs on Request system (http://ccmc.gsfc.nasa.gov). We would like to thank D. L. Mitchell, and J. S. Halekas for their helpful insights.

References

Acuña, M. H., Connerney, J. E. P., Wasilewski, P., Lin, R. P., Anderson, K. A., Carlson, C. W., ... Ness, N. F. (1998). Magnetic field and plasma observations at mars: Initial results of the mars global surveyor mission. *Science*, *279*(5357), 1676–1680. doi: 10.1126/science.279.5357.1676

Andersson, L., Ergun, R. E., Delory, G. T., Eriksson, A., Westfall, J., Reed, H., ... Meyers, D. (2015). The langmuir probe and waves (lpw) instrument for maven. *Space Science Reviews*, *195*, 173–198. doi: 10.1007/s11214-015-0194-3

Arge, C. N., Luhmann, J. G., Odstrcil, D., Schrijver, C. J., & Li, Y. (2004). Stream structure and coronal sources of the solar wind during the may 12th, 1997 cme. *Journal of Atmospheric and Solar: Terrestrial Physics*, *66*(15-16), 1295–1309. doi: https://doi.org/10.1016/j.jastp.2004.03.018

Barabash, S., Lundin, R., Andersson, H., Brinkfeldt, K., Grigoriev, A., Gunell, H., ... Thocaven, J.-J. (2006). The analyzer of space plasmas and energetic atoms (aspera-3) for the mars express mission. *Space Science Reviews*, *126*(1), 113–164. doi: 10.1007/s11214-006-9124-8

Bertucci, C., Mazelle, C., Acuña, M. H., Russell, C. T., & Slavin, J. A. (2005). Structure of the magnetic pileup boundary at mars and venus. *Journal of Geophysical Research: Space Physics*, *110*(A1), A01209. doi: 10.1029/2004JA010592

Bertucci, C., Mazelle, C., Crider, D. H., Vignes, D., Acuña, M. H., Mitchell, D. L., ... Winterhalter, D. (2003). Magnetic field draping enhancement at the martian magnetic pileup boundary from mars global surveyor observations. *Geophysical Research Letters*, *30*(2), 1099. doi: 10.1029/2002GL015713

Brain, D., Barabash, S., Bößwetter, A., Bougher, S., Brecht, S., Chanteur, G., ... Terada, N. (2010). A comparison of global models for the solar wind interaction with mars. *Icarus*, *206*(1), 139–151. doi: https://doi.org/10.1016/j.icarus.2009.06.030

Breus, T. K., Krymskii, A. M., Lundin, R., Dubinin, E. M., Luhmann, J. G., Yeroshenko, Y. G., ... Styashkin, V. A. (1991). The solar wind interaction with mars: Consideration of phobos 2 mission observations of an ion composition boundary on the dayside. *Journal of Geophysical Research: Space Physics*, *96*(A7), 11165–11174. doi: 10.1029/91JA01131

Chattopadhyay, A. K., & Chattopadhyay, T. (2014). *Statistical methods for astronomical data analysis* (Vol. 3). Springer New York. doi: https://doi.org/10.1007/978-1-4939-1507-1

Connerney, J. E. P., Espley, J., Lawton, P., Murphy, S., Odom, J., Oliversen, R., & Sheppard, D. (2015). The maven magnetic field investigation. *Space Science Reviews*, *195*(1), 257–291. doi: 10.1007/s11214-015-0169-4

Crider, D., Cloutier, P., Law, C., Walker, P., Chen, Y., Acuña, M., ... Ness, N. (2000). Evidence of electron impact ionization in the magnetic pileup

boundary of mars. *Geophysical Research Letters*, *27*(1), 45–48. doi: 10.1029/1999GL003625

Dubinin, E., Modolo, R., Fränz, M., Woch, J., Chanteur, G., Duru, F., ... Picardi, G. (2008). Plasma environment of mars as observed by simultaneous mex-aspera-3 and mex-marsis observations. *Journal of Geophysical Research: Space Physics*, *113*(A10). doi: 10.1029/2008JA013355

Dubinin, E., Sauer, K., Lundin, R., Norberg, O., Trotignon, J.-G., Schwingenschuh, K., ... Riedler, W. (1996). Plasma characteristics of the boundary layer in the martian magnetosphere. *Journal of Geophysical Research: Space Physics*, *101*(A12), 27061–27075. doi: 10.1029/96JA02021

Edberg, N. J. T., Brain, D. A., Lester, M., Cowley, S. W. H., Modolo, R., Fränz, M., & Barabash, S. (2009). Plasma boundary variability at mars as observed by mars global surveyor and mars express. *Annales Geophysicae*, *27*(9), 3537–3550. doi: doi:10.5194/angeo-27-3537-2009

Edberg, N. J. T., Lester, M., Cowley, S. W. H., & Eriksson, A. I. (2008). Statistical analysis of the location of the martian magnetic pileup boundary and bow shock and the influence of crustal magnetic fields. *Journal of Geophysical Research: Space Physics*, *113*(A8). doi: 10.1029/2008JA013096

Eparvier, F. G., Chamberlin, P. C., Woods, T. N., & Thiemann, E. M. B. (2015). The solar extreme ultraviolet monitor for maven. *Space Science Reviews*, *195*(1), 293–301. doi: 10.1007/s11214-015-0195-2

Espley, J. R. (2018). The martian magnetosphere: Areas of unsettled terminology. *Journal of Geophysical Research: Space Physics*, *123*(6), 4521–4525. doi: 10.1029/2018JA025278

Garnier, P., Steckiewicz, M., Mazelle, C., Xu, S., Mitchell, D., Holmberg, M. K. G., ... Jakosky, B. M. (2017). The martian photoelectron boundary as seen by maven. *Journal of Geophysical Research: Space Physics*, *122*(10), 10472–10485. doi: 10.1002/2017JA024497

Halekas, J. S., McFadden, J. P., Brain, D. A., Luhmann, J. G., DiBraccio, G. A., Connerney, J. E. P., ... Jakosky, B. M. (2018). Structure and variability of the martian ion composition boundary layer. *Journal of Geophysical Research: Space Physics*, *123*(10), 8439–8458. doi: 10.1029/2018JA025866

Halekas, J. S., Taylor, E. R., Dalton, G., Johnson, G., Curtis, D. W., McFadden,

J. P., ... Jakosky, B. M. (2015). The solar wind ion analyzer for maven. *Space Science Reviews*, *195*(1), 125–151. doi: 10.1007/s11214-013-0029-z

Harada, Y., Gurnett, D. A., Kopf, A. J., Halekas, J. S., Ruhunusiri, S., DiBraccio, G. A., ... Brain, D. A. (2018). Marsis observations of the martian nightside ionosphere during the september 2017 solar event. *Geophysical Research Letters*, *45*(16), 7960–7967. doi: 10.1002/2018GL077622

Holmberg, M. K. G., André, N., Garnier, P., Modolo, R., Andersson, L., Halekas, J., ... Mitchell, D. L. (2019). Maven and mex multiinstrument study of the dayside of the martian induced magnetospheric structure revealed by pressure analyses. *Journal of Geophysical Research: Space Physics*, *124*(11), 8564–8589. doi: 10.1029/2019JA026954

Kutner, M. C., Nachtsheim, C. J., Neter, J., & Li, W. (2005). Simple linear regression. In *Applied linear statistical models* (5th ed., p. 227). McGraw-Hill/Irwin.

Lee, C. O., Jakosky, B. M., Luhmann, J. G., Brain, D. A., Mays, M. L., Hassler, D. M., ... Halekas, J. S. (2018). Observations and impacts of the 10 september 2017 solar events at mars: An overview and synthesis of the initial results. *Geophysical Research Letters*, *45*(17), 8871-8885. doi: 10.1029/2018GL079162

Ma, Y.-J., Altwegg, K., Breus, T., Combi, M. R., Cravens, T. E., Kallio, E., ... Strobel, D. F. (2008). Plasma flow and related phenomena in planetary aeronomy. *Space Science Reviews*, *139*(1), 311–353. doi: 10.1007/s11214-008-9389-1

Matsunaga, K., Seki, K., Brain, D. A., Hara, T., Masunaga, K., Mcfadden, J. P., ... Jakosky, B. M. (2017). Statistical study of relations between the induced magnetosphere, ion composition, and pressure balance boundaries around mars based on maven observations. *Journal of Geophysical Research: Space Physics*, *122*(9), 9723–9737. doi: 10.1002/2017JA024217

Mazelle, C., Winterhalter, D., Sauer, K., Trotignon, J., Acuña, M., Baumgärtel, K., ... Slavin, J. (2004). Bowshock and upstream phenomena at mars. *Space Science Reviews*, *111*(1), 115–181. doi: 10.1023/B:SPAC.0000032717.98679.d0

Mitchell, D. L., Lin, R. P., Mazelle, C., Réme, H., Cloutier, P. A., Connerney, J. E. P., ... Ness, N. F. (2001). Probing mars' crustal magnetic field and ionosphere with the mgs electron reflectometer. *Journal of Geophysical Research: Planets*, *106*(E10), 23419–23427. doi: 10.1029/2000JE001435

Mitchell, D. L., Lin, R. P., Réme, H., Crider, D. H., Cloutier, P. A., Connerney, J. E. P., ... Ness, N. F. (2000). Oxygen auger electrons observed in mars' ionosphere. *Geophysical Research Letters*, *27*(13), 1871–1874. doi: 10.1029/1999GL010754

Mitchell, D. L., Mazelle, C., Sauvaud, J.-A., Thocaven, J.-J., Rouzaud, J., Fedorov, A., ... Jakosky, B. M. (2016). The maven solar wind electron analyzer. *Space Science Reviews*, *200*(1), 495–528. doi: 10.1007/s11214-015-0232-1

Nagy, A., Winterhalter, D., Sauer, K., Cravens, T. E., Brecht, S., Mazelle, C., ... Trotignon, J. G. (2004). The plasma environment of mars. *Space Science Reviews*, *111*(1), 33–114. doi: 10.1023/B:SPAC.0000032718.47512.92

Odstrcil, D. (2003). Modeling 3d solar wind structure. *Advances in Space Research*, *32*(4), 497–506. doi: https://doi.org/10.1016/S0273-1177(03)00332-6

Sauer, K., Bogdanov, A., & Baumgärtel, K. (1994). Evidence of an ion composition boundary (protonopause) in bi-ion fluid simulations of solar wind mass loading. *Geophysical Research Letters*, *21*(20), 2255-2258. doi: 10.1029/94GL01691

Sauer, K., Bogdanov, A., & Baumgärtel, K. (1995). The protonopause: An ion composition boundary in the magnetosheath of comets, venus and mars. *Advances in Space Research*, *16*(4), 153–158. doi: https://doi.org/10.1016/0273-1177(95)00223-2

Vignes, D., Mazelle, C., Rme, H., Acuña, M. H., Connerney, J. E. P., Lin, R. P., ... Ness, N. F. (2000). The solar wind interaction with mars: Locations and shapes of the bow shock and the magnetic pile-up boundary from the observations of the mag/er experiment onboard mars global surveyor. *Geophysical Research Letters*, *27*(1), 49–52. doi: 10.1029/1999GL010703

Xu, S., Liemohn, M. W., Dong, C., Mitchell, D. L., Bougher, S. W., & Ma, Y. (2016). Pressure and ion composition boundaries at mars. *Journal of Geophysical Research: Space Physics*, *121*(7), 6417–6429. doi: 10.1002/2016JA022644